Investigation of $q\bar{q} \to HZ/HW \to \mu^+\mu^- q\bar{q}$ channel at the ATLAS detector at the LHC

Adrian Cross

Student ID number: 1223199

Supervisors: Paul Newman and Paul Thompson

Approximate Word Count:7400

March 2016

Abstract

A search for a 125GeV $H \to \mu^+\mu^-$ decay with an associated production of jets has been performed via the associated production method. This analysis is performed at the current CERN centre of mass energy of $13TeV$ with an integrated luminosity of $100fb^{-1}$. Applying cuts to simulated data has reduced the signal to 22.3% and background to 1.4%. In order to detect $H \to \mu^+\mu^-$ decay at the 95% confidence limit, in the ATLAS detector, the signal must be $35\pm_{10}^{13}$ times larger than the Standard Model prediction. This puts an upper limit on the branching ratio of $H \to \mu^+\mu^-$ of $7.665 \pm_{2.19}^{2.85} *10^{-3}$.

Contents

1 Introduction

1.1 Higgs Theory

The Higgs field corrects several aspects of modern particle physics involving the electroweak and strong interactions. While these mechanisms accurately predict the existence of four bosons in total, $Z^0, W^\pm$ and photons, they are also predicted to be massless when experimentally only the photon is found to be massless. The Higgs mechanism corrects for this via electroweak symmetry breaking, where the bosons couple to the Higgs field except for the photon, giving them mass while retaining normalisability.

The Higgs field is scalar and has a non-zero vacuum expectation value, meaning that it permeates all space. This is important as it explains how fermions have a non zero mass. As fermions move through the Higgs field they interact with it, acting like they are travelling through a medium giving them their mass. The mass of fermions depend on the Yukawa coupling to the Higgs field[17]. Supersymmetric models predict the possible existence of other Higgs bosons, Higgsinos, with a different mass than the conventional Higgs boson. These models are based on the premise that each boson has a supersymmetric fermionic partner, and vice versa. Currently no such particle has been seen experimentally however certain models have been constrained and discounted. Different supersymmetric models predict both different properties and number of supersymmetric particles which is an important consideration when experimentally searching for such particles parameters[15].

The Higgs boson mediates the Higgs field. When first searches were underway the Higgs mass was unknown, however it was bound by the Z and top mass via direct reconstruction, giving it a mass $m_H < 200 GeV$. The Higgs mass is also bound indirectly by theoretical Standard Model interpretation of currently known particle properties [6]. The Higgs boson mass is an important consideration as it generally decays to the heaviest particle that is energetically allowed as it couples to the mass of decay products. This makes discovery difficult as the background now depends on an unknown quantity, requiring detailed analysis at different Higgs masses each with different decay cross sections dependent on the Higgs mass. Using this method the Higgs boson particle was found in 2012 with a mass of $\approx 125 GeV/c^2$[6]. this has now been refined to $125.09 \pm 0.21(stat) \pm 0.11(syst) GeV/c^2$[4]. Current experiments indicate that the Higgs boson has a parity of $+1$, a spin of 0, a neutral electric and neutral colour charge.

1.2 Higgs Boson Production

The Higgs boson can be produced via several different production channels, shown in figure 1. At the ATLAS experiment gluon gluon fusion, mediated by a top quark, is the dominant process with a cross section roughly an order of magnitude higher than the other processes due to the high levels of gluons produced in proton-proton collisions[16]. This production method will only produce the decay products of the Higgs boson and no associated particles. In gluon and vector boson fusion the production cross section is dependent on the mass of the particles producing the Higgs boson, due to the Higgs boson coupling to mass. During these two processes the Higgs boson is produced alongside two quarks being produced which are seen as jets in the detector due to QCD confinement. The associated production method will produce both the decay product of the Higgs and the decay products of the vector boson, which is typically two quarks seen as hadronic jets. For this project the associated production method has been concentrated on with the vector boson decaying to quarks (see section 1.4).
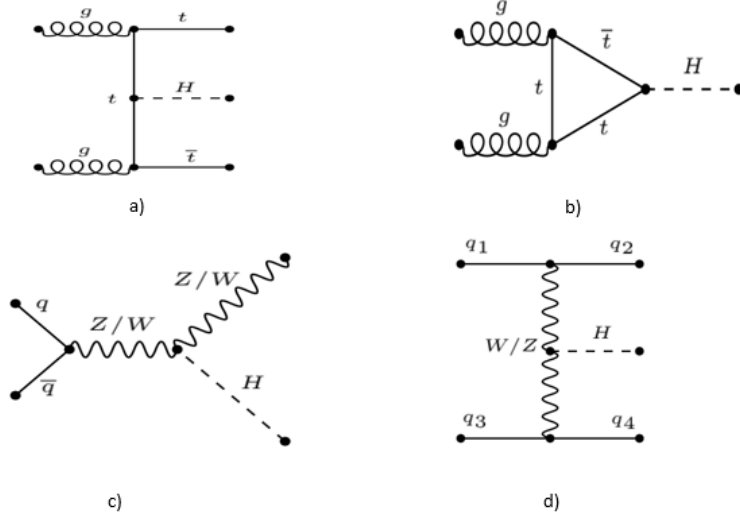
Figure 1: Higgs boson production channels, a) is associated production of $t\bar{t}$ pair (cross section 0.5085pb), b) is gluon-gluon fusion (cross section 43.92pb), c) is associated production of a vector boson (cross section 2.2496pb) and d) is vector boson fusion (cross section 3.748pb) [6][12].

1.3 Higgs Boson Decay

The Higgs boson has been observed, at the CMS and ATLAS experiment, via several different decay channels. The requirement for a confirmed detection is a significance of 5 standard deviations. Several decay channels currently being investigated are shown in figure 2.
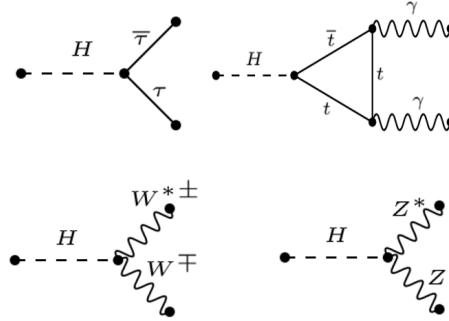

Figure 2: Higgs boson decay channels, the double photon decay can also be mediated by W bosons [4][6][12].

Currently $H \to \tau\bar{\tau}$ has a significance of 3.7σ [14], while the other decay channels have all been confirmed at 5σ. The particles produced decay into varying particle detected using the ATLAS detector. The momentum and energy of these produced particles are measured and used to reconstruct the interaction in order to measure the Higgs boson properties as well as how it decays. For this project the currently unseen decay $H \to \mu^+\mu^-$ decay will be investigated.

4

1.4 $\quad q\bar{q} \rightarrow HZ/HW \rightarrow \mu^+\mu^- q\bar{q}$ Channel

The $H \rightarrow l^+l^-$ decay has only been observed via tau leptons. This due to their higher mass relative to muons and electrons, meaning they have an increased branching ratio as the probability for Higgs boson decay is proportional to the product of the mass of produced particles. Equation 1 shows the τ decay channel to be 283 times more likely than the μ channel making it much more difficult to detect.

$$\frac{\sigma(H \rightarrow \tau^+\tau^-)}{\sigma(H \rightarrow \mu^+\mu^-)} = \frac{M_\tau^2}{M_\mu^2} \approx 283 \tag{1}$$
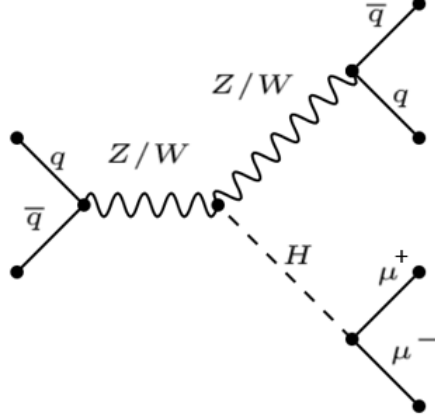

Figure 3: Higgs production and decay mode being investigated

The double muon decay corresponds to a small branching ratio of $2.19 * 10^{-4}$ however the decay of the Higgs boson is a clean decay allowing a better sensitivity relative to the tau leptons. This is due to the tau leptons being able to decay to hadrons which are more difficult to detect whereas the muons are directly detected via the Inner Detector and the Muon Spectrometer. This decay tests whether the Higgs boson decay is proportional to the lepton mass, by comparing the experimentally derived branching ratios for leptons and muons, or another property. This also facilitates an investigation of the Yukawa coupling in second generation fermions which is an important part of understanding electroweak symmetry breaking in the Standard Model[17][20]. An analysis of this channel is performed using simulated data in a C++ based ROOT format [13] using the ATLAS detector.

2 Atlas Detector

2.1 Inner Detector

The Inner Detector of the ATLAS experiment consists of three distinct layers and is closest part of the detector to the beamline. This section of the detector is designed to combine measurements from high-resolution trackers in order to track charged particles from the interaction point as they pass through it and thus measure charged particle momenta. The Inner Detector covers a range of $|\eta| < 2.5$ and the total range of ϕ. The momentum resolution is $\frac{\sigma_{p_T}}{p_T} = 0.05\% p_T GeV \oplus 1\%$[3].

The first layer, closest to the beamline, is a silicon pixel detector which covers a radial distance of 50.5mm to 150mm. There are 1744 individual pixel modules covering an area of 16.4mm * 60.4mm each. These modules contain a total of 47232 pixels and each of these pixels have dimensions of $50\mu m * 400\mu m$. These modules are arranged concentrically around the beamline with three layers in the barrel region and two in the end-caps of three disks each. As a charged particle passes through a pixel a hit is registered and read out by one of the 16 radiation-hard front end chips, as long the signal exceeds a tunable threshold. This region, being the closest to the beamline, has been designed to take the most accurate measurements of particle position while being the most radiation hardened due to the high flux of particles travelling through this region [3].

The next layer is the SemiConductor Tracker (SCT) which covers a radial distance of 299mm to 560mm. Instead of pixels this detector uses 4088 modules of silicon strip detectors arranged concentrically with four in the barrel and two in the end-caps of nine discs each. The strips in the barrel are approximately parallel to the solenoid with a small pitch of $80\mu m$ on them, in the end cap they are arranged radially with a variable pitch. The modules contain four silicon strip sensors which are daisy chained together to give 768 strips, 12cm in length. Typically a charged particle will be detected by eight strips, four point measurements, as it passes through this region. The readout is similar to the pixel detector, using radiation-hard front end readout chips, in that a hit is determined if the signal is above a pre-defined, variable threshold. [3].

The Transition Radiation Tracker (TRT) is the final layer contained within the Inner Detector which covers a radial distance of 563mm to 1066mm. This is a straw detector consisting of 298304 proportional drift tubes. These tubes contain gas with a composition of xenon gas(70%, carbon dioxide(27%) and molecular oxygen(3%). As charged particles pass through these straws they ionise the gas inside which is then read out by 350848 channels of electronics. In the barrel the straws are arranged in three cylindrical layers whereas in the end cap they are arranged radially outwards in 80 modular structures. Particles with a transverse momentum $P_T > 0.5 GeV$ and pseudorapidity $|\eta < 2.0|$ cross approximately 30 straws as they pass through this region. The TRT can also identify when electrons pass through due to the polypropylene fibres between the straws as they deposit a larger amount of energy compared to other particles passing through [3].

2.2 Superconducting Magnet System

The first part of the magnet system is a solenoid which encloses the Inner Detector with a length of 5m and an inner diameter of 2.4m. This produces a central magnetic field of 2T and a peak magnetic field of 2.6T throughout the Inner Detector facilitating the bending of charged particles. The solenoid thickness has been minimised as much as possible thus improving the performance of the calorimeters as less particles, and particle energy, are lost when travelling through this section and therefore more is deposited in the calorimeters. The cooling system consists of helium cooled to 4.5k and is shared with the electromagnetic calorimeter (see 2.3), in order to reduce solenoid thickness. The superconducting cables are a composite material containing a varying ratio of niobium-titanium and copper with an aluminium stabiliser with a rectangular cross section [9].

The toroidal magnets are arranged radially and symmetrically around the beam axis to produce a variable magnetic field, shown in figure 4 throughout the muon detector. This facilitates precise muon momentum measurements in the muon detector. There are eight barrel and two end-cap toroidal magnets[9].
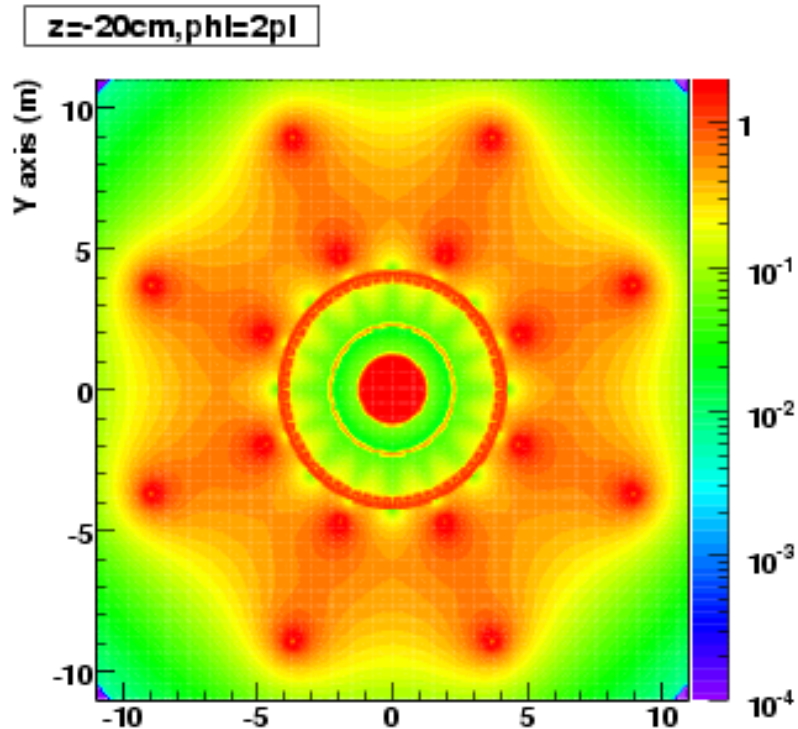
Figure 4: Simulated magnetic field in the ATLAS detector along the z direction taken from [1].

2.3 Calorimeters

The electromagnetic calorimeter (ECAL) is a sampling calorimeter designed to measure the energy of electrons, positrons and photons which are deposited and measured in this region. The passive material used in the ECAL is lead which causes a particle shower, via bremsstrahlung and pair production, when one of these particles enters the region. The energy from these showers is deposited in the liquid argon (LAr) active medium where it can be electronically read out. In the pseudorapidity range $|\eta| < 1.8$, before the main part of the calorimeter there is a LAr instrumented presampler which is used to correct for energy loss in the material which occurs further up in the ECAL[9]. The barrel region of the ECAL covers a range $|\eta| < 1.475$ and has a thickness of ≈ 24 radiation lengths (X_0) with alternating lead and LAr layers. The endcap region covers a range $1.375 < |\eta| < 2.5$ with a thickness of $\approx 26 X_0$. The overall energy resolution for the ECAL is $\frac{\sigma E}{E} = \frac{10\%}{\sqrt{E}} \oplus 0.7\%$[10][9][5].

The hadronic calorimeter (HCAL) is a sampling calorimeter that lies beyond the ECAL and is designed to measure the energy of hadrons and jets which is deposited and measured in this region. The barrel HCAL is a sampling calorimeter consisting of plastic scintillator tiles as the active medium, steel as the passive material and has a range $|\eta| < 1.7$. The endcaps have a pseudorapidity range of $1.5 < |\eta| < 3.2$. LAr calorimeters are used for the HCAL end-caps however these use copper as the passive medium rather than lead. The energy resolution for the barrel and end caps is $\frac{\sigma E}{E} = \frac{50\%}{\sqrt{E}} \oplus 3\%$[10]. The forward calorimeters is the part of the HCAL closest to the beam-line, $3.1 < |\eta| < 4.9$, thus requiring it to be more resistant to radiation due to a higher flux of

7

particles. This region contains three sections, the first is an LAr calorimeter with copper as the passive material while the last two use tungsten. The energy resolution of the forward calorimeter is $\frac{\sigma E}{E} = \frac{100\%}{\sqrt{E}} \oplus 10\%$[10] [9][5].

2.4 Muon Spectrometer

The muon detector is the final part of the ATLAS detector lying beyond the HCAL. The muon detector is located here as muons are highly penetrative particles and most will pass through the calorimeters whereas other particles will be blocked by the calorimeters. The muon momentum measurement is facilitated by a variable magnetic field generated by toroidal magnets (see 2.2). This region contains two main parts, precision chambers, which measures muon position to a high precision, and trigger chamber which measure the time resolution of muons to a high precision.

The first section the muons pass through is the monitored drift tube chambers (MDT). This chamber contains hollow aluminium tubes with an outer tube diameter of $30mm$ and are filled with a gas mixture of argon (91%), methane (5%) and molecular nitrogen (4%) at a pressure of 3 bar. In the centre of these tubes is a thin wire passing through. As muons penetrate these tube they ionise the gas inside. These ionise particles then drift to the outside of the tube as well as the central wire which is then read out by an amplifier. These tubes are stacked on top of each other contained within a support structure [11].

The cathode strip chambers (CSCs) are the next part of the muon detector precision chambers and are based on a wire chamber setup. As the muon travels through a gas, which is a mixture of argon, carbon dioxide and Tetrafluoromethane, filled central region it ionises the surrounding particles. These particles are then attracted to either the anode or the cathode. The overall charge induced by the particle is measured by these strips and read out [11].

The next two muon chambers are part of the ATLAS trigger system providing a binary output. The resistive plate chamber (RPC) with a space time resolution of 1cm *1ns facilitating the distinction between different collision events. Inside the RPC there is a thin band containing tetrafluorade and isobutane with two parallel resistive bakelite plates either side with an electric field, of strength $4.5kVmm^{-1}$, between them. as charged particles enter this electric field they ionise the gas producing a signal, read out by metal strips on both sides of the detector. There are two layers of the RPC, one of which is orientated parallel to the MDT whereas the other is perpendicular providing a coordinate measurement [11] [9].

The thin gap chambers are the last part of the ATLAS detector and are contained within the end-cap. These are also multi-wire chambers with a much thinner gap of 2.8mm filled with carbon dioxide and n-pentane and work by ionising the gas inside the gap in the same way as the CSCs [11].

The overall momentum resolution for the muon chamber is typically $\frac{\sigma p_T}{p_T} = 3\%$ for lower momentum muons rising to approximately 10% for a momentum of $1TeV$[11].

2.5 ATLAS Trigger System

The overall amount of data collected by the ATLAS detector is $\approx 10^9 Hz$ at a luminosity of $10^34cm^2s^{-1}$ which must be reduced to $\approx 100Hz$ in order to store and analyse effectively. This is

achieved by the ATLAS trigger system which reduces the overall information readout by excluding events while retaining the events of interest such as Higgs boson production and rare supersymmetric events. The trigger system is arranged in three levels [18].

The first level is determined at the hardware level to reduce the output to $\approx 10^5 Hz$ in less than $2.5\mu s$. This stage relies mainly on information from the muon triggers and electronics, the field-programmable gate array, within the calorimeters [18]. The second trigger uses information from both the first trigger, which identifies regions of interest, and the readout chips to find physics objects. At this level the data rejected is determined at the software level to reduce the data down to $\approx 10^3 Hz$. The final trigger is also software based which selects the events of possible interest for long term storage[9].

2.6 Luminosity

The LHC attempts to maximise the amount of luminosity it can in order to make new particle physics discoveries. It does this by first of all maximising the centre of mass energy, currently at $13TeV$, maximising the number of protons in each bunch, minimising the time between collisions and minimising the cross section of the bunches. It is important to distinguish between different collisions therefore there is a minimum time between bunch crossing, determined by the time resolution of the detectors[21].

The LHC has had several different runs and different centre of mass ($\sqrt{s}$) energies. The integrated luminosity is a measure of the total number of events being collected. Certain physical processes being investigated, such as the $H \rightarrow \mu^+\mu^-$ process, will require a certain amount of integrated luminosity in order to confirm that the process has occurred by differentiating it from the background. ATLAS originally ran at $\sqrt{s} = 7TeV$ where it collected a total integrated luminosity of $7fb^{-1}$ moving up to $\sqrt{s} = 8TeV$ with an integrated luminosity of $7fb^{-1}$. This project concentrates on the current run at the LHC which has a $\sqrt{s} = 13TeV$ with $\approx 3fb^{-1}$ being collected so far. In the future LHC high luminosity stage there is scope to collect up to $3000fb^{-1}$ of data. The analysis will be based on $100fb^{-1}$ of total data being collected at this energy[21].
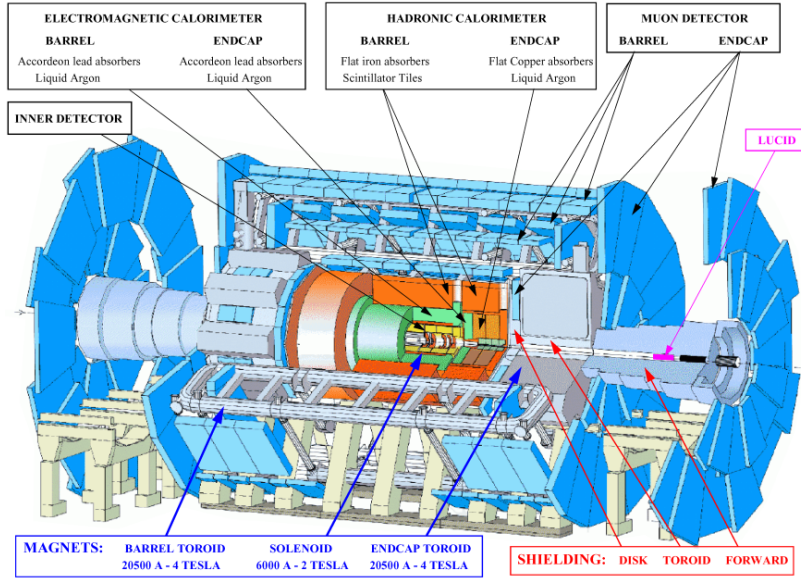
Figure 5: ATLAS detector cross section [2].

3 Simulating Data

Data for this decay, along with its associated background, has been simulated using Monte Carlo simulation. Monte Carlo simulations work by continually simulating what particles are created during a proton proton collision in the LHC using random numbers. The quantities and methods by which the various particles are created and decay is dependent on the cross sections and branching ratios of particle, determined for a $\sqrt{s} = 13 TeV$ collision. The result of this simulation is a series of resonance peaks, mainly the Z boson, W boson and Higgs boson, corresponding to the various invariant masses of particles being created and decaying. For the channel investigated in this project, figure 3, the processes for signal and background events have all been simulated using Monte Carlo software[24]. The Monte Carlo events have been weighted by a number to account for next to leading order contributions. For most events,which are leading order, this weighting is one however, for next to leading order contributions, this number can be a positive or negative number depending on the contribution.

The events generated using Monte Carlo software does not include any simulation on the ATLAS detector. In reality the resonance peaks will be wider, due to experimental uncertainty, and the detector will include some bias on particle detections. The Geant4 program[8] simulates the passage of particles through various types of matter and is suitable for detector simulations. It simulates many different hadronic, electromagnetic and leptonic interactions between the particles from the proton proton collision and the particles which make up the detector. These interactions are dependent on both the parts of the detector being traversed and the particles properties (momentum etc.). Figure 6 is a plot of muon transverse momentum and pseudorapidity showing a 'hole', region where significantly less particles are detected due to detector inefficiencies. For the different types of background and signal there are a certain number of events in the N-tuple. All of these events need to have the same luminosity therefore a 'Lumiweight' is applied to each background based on

their cross section. The signal has been scaled downwards, as there is a larger number of Monte Carlo events than actual events, and all of the background events have been scaled upwards.
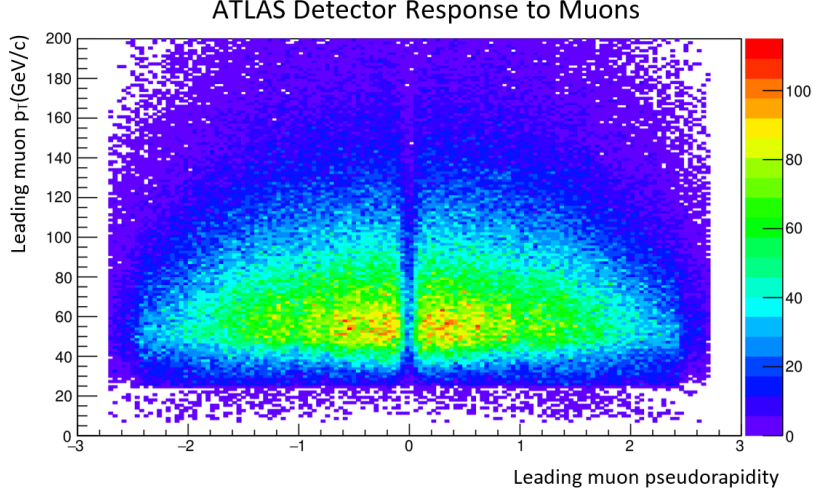

Figure 6: Leading muon transverse momentum against pseudorapidity showing an area of low detector efficiency.

4 Muon Resolution Simulation

By looking at the Monte Carlo data, which has been put through a Geant4 ATLAS simulation, properties of the ATLAS detector can be deduced. The muon resolution of the ATLAS detector varies depending on the transverse momentum of the muons. The muons have first been binned in terms of their transverse momentum, with a larger bin at high transverse momentum to account for low number of events which can cause large statistical fluctuations. For each bin a histogram of the muon invariant mass is generated which has a Gaussian peak, due to experimental error, around the $125 GeV$ Higgs boson peak. This peak has an associated standard deviation which represents the muon resolution. Figure 7 shows how the muon resolution varies with transverse momentum.

Figure 7: Muon resolution varying with muon transverse momentum

A fit has been made on figure 7 which attempts to parameterise the overall detector response to the momentum of the muons. This fit is based on Equation 2[22].

$$\frac{\sigma p_T}{p_T} = \frac{A}{p_T} \oplus \frac{B}{\sqrt{p_T}} \oplus C \tag{2}$$

Where A,B and C vary depending on the fit. The muon resolution depends on both the properties of the muon detector, efficiency etc., and the Inner Detector track length which depends on the pseudorapidity. From this fit it is found that the simulated resolution closely matches the actual resolution of the ATLAS detector[22].

5   Sources of Background

There are a significant number of background events which prevent the signal peak from being seen in the ATLAS detector. Figure 8 demonstrates this by showing the signal plotted with all the different background events in the signal range.
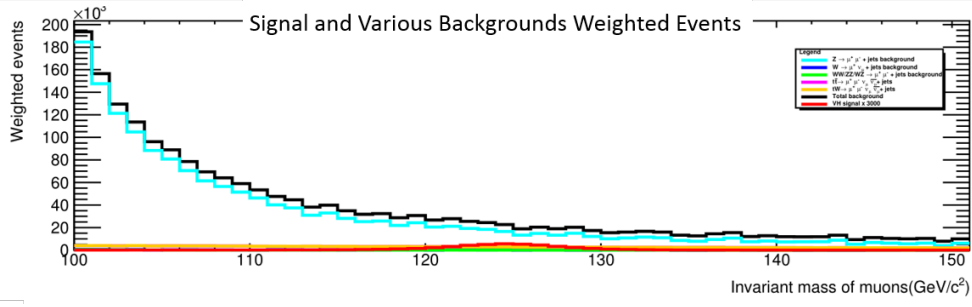
Figure 8: Plot of muon invariant mass against weighted events for the signal and various backgrounds.

The dominant source of background is caused by Z bosons decaying to muons, mostly via the Drell-Yan process, with associate jet production as shown in figure 9[7]. The invariant mass of the muons will peak at the Z mass, $91 GeV/c^2$, which dominates over the signal which peaks at the Higgs boson mass, $125 GeV/c^2$. This background has no missing transverse energy and similar jet events to the signal but a slightly higher transverse muon momentum peak, making it hard to discern from this background[7].

Other sources of background which have been included in the analysis are the misidentification of a W boson decaying to $\mu^+\mu^-$ with an associated production of jets; Di boson background where two bosons decay to opposite muon neutrino pairs with an associated production of jets; $\bar{t}t$ background where top quarks decay into W bosons,which decays to a muon neutrino pair, and a bottom quark, which appears as jets in the detector[7]; the single top background involving a top quark and a W boson interacting to form $\mu^+\mu^-$ and $\overline{\nu_\mu}\,\nu_\mu$. The background is vastly greater than the signal so in order to observe signal events the background needs to be reduced.
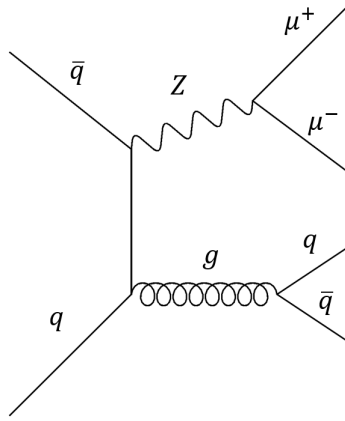

Figure 9: One of the Feynmann diagram of the most dominant background process of Z decaying to muons with associated production of jets[12][7]

6 Cuts

The current simulated data set has a large amount of background relative to the signal. The number of signal events compared to the number of background events can be increased by only accepting events where certain detected particles have certain variables, such as spatial coordinates, or combination of these variables. An example is shown in figure 10 where only event with $70 GeV/c^2 \leq m_j ets \leq 95 GeV/c^2$ are accepted and the rest are rejected. Cuts can accept particles in a range below the cut value, above the cut value or between a lower and an upper cut, depending on the particle and variable being cut. In order to determine the cut type the shapes of signal and background histograms can be plotted. Where these variables are measured for different particles in the ATLAS detector is summarised in section 2. The cuts for these variables are applied sequentially so values for signal and background retained are on all cuts up to the current one.
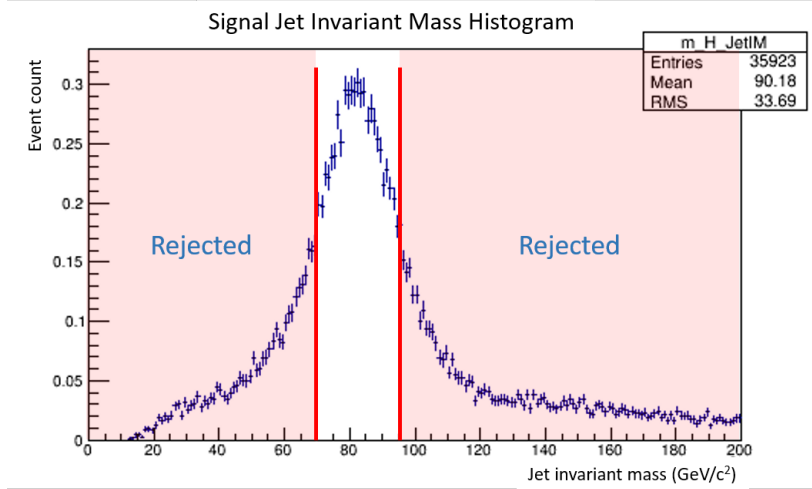

Figure 10: An example of how a cut is performed on the sum of invariant mass of jets.

6.1 Preselection Cuts

Before the data is fully analysed there are several preselection cuts it has gone through. These are events which are obviously not the signal so are removed before being processed, reducing processing time. The first requires that the event contain exactly two muons and greater than two jets. This requirement is motivated by the Feynmann diagram shown in figure 3. More than two hadronic jets are required due to next to leading order processes where gluons can be radiated which decay into additional hadronic jets. Preselection cuts made to the Monte Carlo data are that the transverse momentum of the jets must be greater than $20 GeV/c^2$ and the pseudorapidity of particles must be less than 2.5.

6.2 Determining Cuts

The optimum cuts on particles are determined by calculating the significance for a variety of different cuts. The equation to calculate the statistical significance, for large amounts of data, is shown in equation 3[23]. This significance is introduced in order to quantify the probability that an observation

was a statistical fluctuation rather than an actual measurement. An example of this is shown in figure 11 where the algorithm begins by calculating a significance for a cut value of $3GeV$, accepting data only above that value, and subsequently does the same for 4GeV, then 5GeV etc. This significance has then been plotted against the cut value and peaks at the optimum cut value.

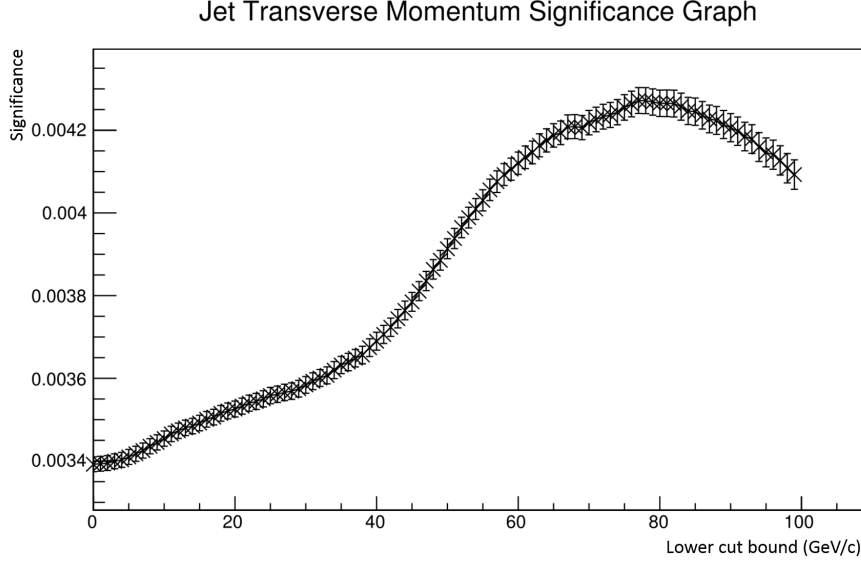$$Significance = \frac{Signal}{\sqrt{Background}} \tag{3}$$

Figure 11: Signal over square root background for the transverse momentum of the vector boson showing the optimum cut value.

There are some possible sources of error with this approach. The error on the graph shown in figure 11 is relevant for significance graphs where the peak is not well defined. In this case the actual optimum cut value could exist somewhere within a wide area on the changing variable variable. Another source of error is caused by correlation between the variables being cut on. While this is not a problem for many of the cuts when a large number of cuts are being performed sequentially it can have a significant affect on the optimum cut value. Due to the low number of signal events this treatment could overestimate the significance [23].

6.3 Polar Angle in the Transverse Plane (ϕ)

The first cuts made were on the difference between particles ϕ value, $\Delta\phi$. ϕ is defined as the angle around the beamline in the transverse plane. The absolute value of ϕ remains mostly constant for particles being created however cutting on $\Delta\phi$ can prove useful. The particles for which the angle between them is being cut are the Higgs and vector boson. $|\Delta\phi| > 2.6$ for which the signal retained is 85.1% and the background retained is 63.4%.

6.4 Pseudorapidity (η)

Pseudorapidity is a coordinate that describes the angle of the particle to the beamline. It is a logarithmic scale which is ∞ when parallel to the beam axis and zero when perpendicular. The pseudorapidity of a particle will determine what parts of the detector it will travel through, barrel or end cap see section 2, therefore it has a large effect on the resolution to which its properties are measured. Cuts have been made on the difference between absolute pseudorapidity values ($|\Delta\eta|$) on the Higgs and vector bosons where $|\Delta\eta(HV)| < 1.7$ retaining 71.2% signal and 31.2% background.

6.5 Transverse Momentum (p_T)

The transverse momentum is defined as the momentum of the particles perpendicular to the beam axis. The momentum of the particles in the beam line is unknown but the p_T value will sum to zero, as their is no initial momentum in this direction, facilitating event reconstruction. In this analysis the p_T of the vector boson, using the momentum of the jets, and the muons, by using the momentum of the Higgs boson, has been cut on with $p_T(V) > 77 GeV/c^2$ retaining 63.9% signal, 20.1% background and $p_T(H) > 76 GeV/c^2$ retaining 60.5% signal, 18.7% background.

6.6 Missing Transverse Energy (MET)

MET is the energy not picked up when particles deposit energy in the calorimeter and is only in the transverse plane due to the beam momentum being unknown. This is found by taking all particles involved in the interaction and reconstructing them to see what energy is missing. Larger values of MET are indications of neutrinos, which are not produced in the proposed signal channel, which leave the detector without being detected. Another possible source of MET are supersymmetric candidates which cannot be detected by the ATLAS detector [7]. Much of the MET is caused by some of the energy not being picked up in the calorimeter due to detector effects. The cut on MET is $MET < 53 GeV$ retaining 55.2% signal and 17.0% background.

6.7 Invariant Mass of the Vector Boson

The ATLAS detector can make measurements on the invariant mass of the jets passing through it. Using the jet invariant mass the invariant mass of the Z boson decaying can be determined. The cut made on the jet invariant mass was performed by first taking a central value around the W/Z resonance peak, 83GeV. A 'cut width' is then applied where the lower bound of the cut is the central value minus the cut width and the upper bound is the central value plus the cut width. Subsequently increasing the cut width and calculating the significance for particles within these bounds has been used to determine the optimum cut value. The cut on the invariant mass of the jets is that it must be between $61 GeV \leq m(jets) \leq 105 GeV$ retaining 32.0% signal and 2.7% background.

6.8 Two Dimensional Cuts

Instead of the method used in section 6.7 to cut on the jet invariant mass a 2 dimensional cut can be applied which has a different upper and lower limit. This works by first starting with a lower limit of $3 GeV/c^2$, looping over all the upper limits and then increase the lower limit, starting the process over again. A graph showing the fraction of signal retained is shown in figure 12.
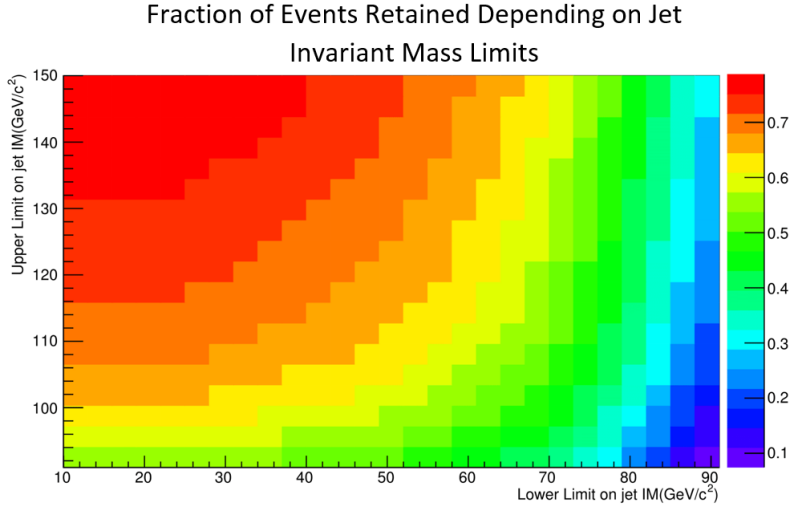
Figure 12: Graph showing how much signal is retained depending on lower and upper cut values.

In practise this method greatly increases the computing power required, approximately an order of magnitude increase, without cutting any more background relative to the signal. Therefore, for this analysis, the method outlined in section 6.7 was used.

6.9   Refining Cuts

Due to the possible errors on the optimum cut values they require further investigation. In order to further refine the cuts the various cut values have been systematically adjusted. Each time they are adjust the confidence limit for distinguishing the signal and signal plus background is calculated; see section 8.1 for details on how the confidence limits are calculated. The confidence limit indicates how well the signal can be distinguished from the background events, therefore if this value increases when adjusting cuts it is an improvement. The value of the cuts are continually altered until a confidence limit maximum is found which is the optimum cut value. This analysis has been performed for each of the cuts and is summarised in table 1.

Cut made	Signal retained	Background cut
$|\Delta\emptyset(HV)|>2.8$	79.7%	49.1%
$|\Delta\eta(HV)|<1.7$	65.7%	24.8%
$p_T(Jets)>50GeV/c$	56.7%	16.8%
$p_T(Muons)>50GeV/c$	53.6%	13.2%
MET<40GeV	46.3%	10.5%
$70GeV\leq IM(Jets)\leq96GeV$	22.3%	1.4%

Table 1: Table showing the final cuts that have been applied to the Monte Carlo data.

17

6.10 Cut Outcome

Performing these cuts has reduced the background to 1.4% of its original value with a background of 22.3%. Figure 13 shows the weighted events against muon invariant mass plot after the cuts are applied.
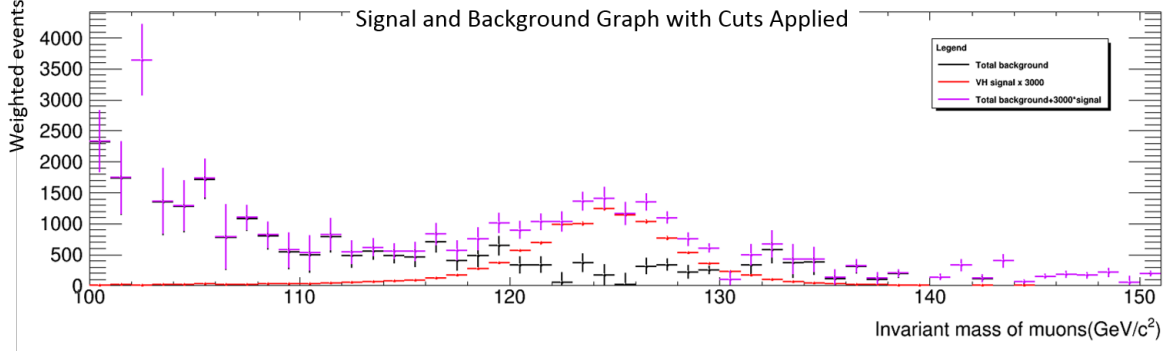

Figure 13: Graph of weighted events against muon invariant after cuts have been applied.

From figure 13 it can be seen that the signal relative to the background has been greatly increased. Due to the fact that there is now a smaller Monte Carlo data set the statistical fluctuations have increase. These fluctuation have been reduced using methods outlined in section 7.

7 Systematic Errors

The Monte Carlo data systematic uncertainties need to be considered for a complete analysis. Systematic uncertainties are the unknown variations in the number of weighted events caused by unknown effects in either the detector or Monte Carlo simulations. Sources of systematic uncertainties in the detector include the efficiencies of the muon trigger, event reconstruction, particle identification, muon momentum scale and resolution[7].Sources of systematic error on the Monte Carlo simulation include theoretical uncertainty on the branching ratio of the $H \to \mu^+ \mu^-$ decay originating from the uncertainty on the Higgs boson mass[20].

In order to estimate the uncertainties the histogram of weighted events against muon invariant mass is taken and plotted. A plot of the Breit-Wigner function is taken and fitted to the background data. The Breit-Wigner function, shown in equation 4[20], is used to fit to particle resonances, in this case the Z resonance present in the background events.

$$f(m_{\mu\mu}) = \frac{\beta}{(m_{\mu\mu} - m_Z)^2 + \gamma^2/4} \tag{4}$$

Where β is a constant, $m_{\mu\mu}$ is the muon invariant mass, m_Z is the mass of the Z boson ($91 GeV/c^2$) and γ is the the width of the resonance peak. Due to these systematic uncertainties the Breit-Wigner does not accurately map the total background. Instead equation 5, which is a corrected equation taken from[20], is used which corrects for the various backgrounds and makes estimates of the systematic uncertainties[20].

$$f(m_{\mu\mu}) = \frac{C_1 * \beta * e^{-\lambda * m_{\mu\mu}}}{(m_{\mu\mu} - m_Z)^2 + \gamma^2/4} + \frac{(1 - \beta) * C_2 * e^{-\lambda * m_{\mu\mu}}}{m_{\mu\mu}^2} \tag{5}$$

Where C_1 and C_2 are normalisation constants and λ is a variable. Another estimate of the systematics can be made by using the original Monte Carlo data and the smooth function which attempts to reduce the statistical fluctuations, which can bee seen in figure 10. A plot showing all of these fits is shown in figure 14. An estimate of the systematics can now be made by taking the difference between the corrected fit, shown in equation 5, and the Breit-Wigner fit and add it in quadrature to the smoothed Monte Carlo, for each data point. Using this method the systematic errors are found to be between 4% and 40% in the region $100 GeV/c^2 < m_{\mu\mu} < 150 GeV/c^2$. If this procedure is applied to only the Breit-Wigner and corrected fit the systematic errors are between 0% and 20% in this region. This systematic error appears to be similar to the systematics found in [20].
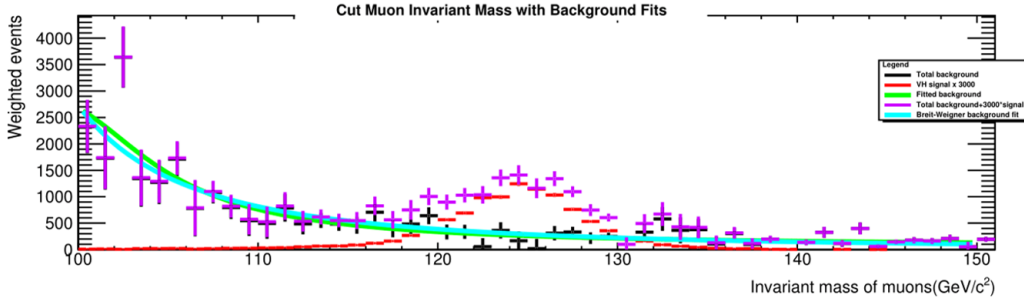

Figure 14: Graph showing various fits to the Monte Carlo background in order to estimate the systematics.

8 Results

8.1 Signal Required

Confidence limits are used to calculate whether the signal is statistically different from the background in order to see a result. Equation 6 is used to calculate the confidence limit. This confidence limit is calculated using the TLimit function which adopts a semi-bayesian method[19][13].

$$CL = \int_x^\infty P(x) dx \tag{6}$$

Where $P(x)$ is the probability density function. This integrates up to a given value of the test statistic which is the expected test statistic for both the signal plus background ratio and the background only hypothesis. The TLimit function does this by using a set of Monte Carlo experiments, for this analysis 50000 are used, in order to compute the limit[19][13]. The signal is then scaled up relative to the Standard Model scaling by a signal scale factor. As this scales up it separates the signal plus background and the background only hypothesis until they are separated at the 95% confidence limit. Figure 21 shows how the confidence limit changes with the signal scaling.
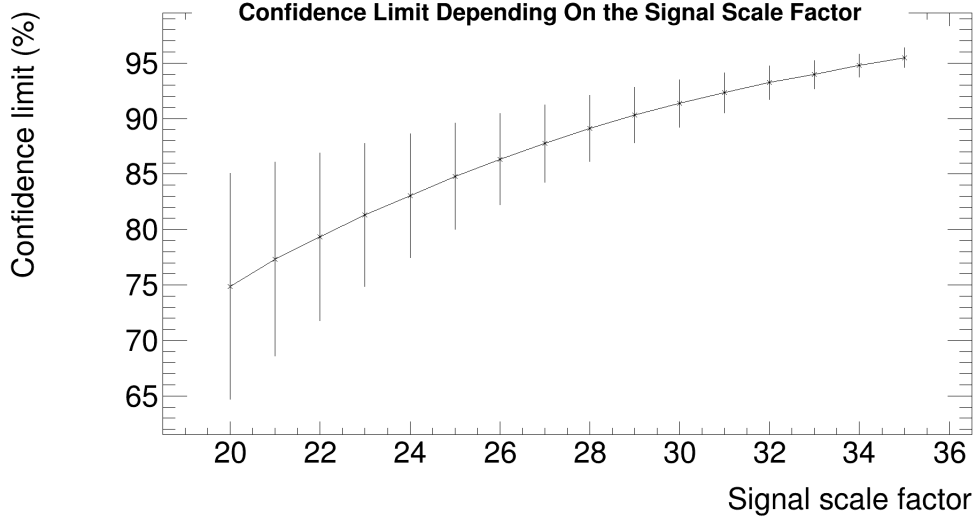
Figure 15: Graph showing how the confidence limit varies depending on the scale of the signal relative to the Standard Model

This graph shows that as you increase the signal scale factor the the confidence level increases. At a signal scale factor of $35\pm^{13}_{10}$ a confidence limit of 95% (2σ)is obtained. This puts an upper limit on the branching ratio of $H \rightarrow \mu^+\mu^-$ of 7.665 $\pm^{2.85}_{2.19} *10^{-3}$. Therefore the signal is required to be $35\pm^{13}_{10}$ times the Standard Model, by having a branching ratio of $35\pm^{13}_{10}$ times the Standard Model, in distinguish between background and signal at the 95% confidence limit. Therefore, if the Standard Model is obeyed, this decay will not be seen.

8.2 Alternatives to the Standard Model

There are several ways in which the Standard Model could be wrong and therefore this decay could be seen. One of these ways is if equation 1 is incorrect. This would mean that the interplay between flavour physics and electroweak theory and different models of this could produce a Higgs boson which does not behave like a Standard Model Higgs boson[17].

The Higgs Boson which was discovered at $125GeV$[6] could be one of many possible Higgs bosons according to some supersymmetric models. In these models the Higgs boson has a supersymmetric counterpart, the Higgsino, which has different properties than the Higgs Boson. The observed 125GeV Standard Model Higgs boson could actually be a supersymmetric Higgsino where actual Standard Model Higgs boson would be undiscovered and have a different mass, however current, ongoing experiments at the LHC seem to indicate Standard Model properties of the $125GeV$ Higgs boson[15].

9 Summary and Conclusions

Using simulated data from Monte Carlo simulator and a Geant4 detector simulator a value for the required signal scale factor of $H \rightarrow \mu^+\mu^-$ relative to the Standard Model branching ratio has been

determined as $35\pm^{13}_{10}$ at the 95% confidence limit for $100fb^{-1}$ of luminosity. This puts an upper limit on the branching ratio of $H \to \mu^+\mu^-$ of $7.665\pm^{2.85}_{2.19}*10^{-3}$. Therefore, if the Standard Model is obeyed, this decay will not be seen unless a non Standard Model process causes the Yukawa coupling to differ from being proportional to the mass of the decay products(see section 8.2. This value of the signal scale factor has been determined by first investigating possible cuts on the variables of the particles produced. Using cuts on transverse momentum, polar angle in the transverse plane, pseudorapidity, jet invariant mass and missing transverse energy the background has been cut to 2.7% of the original while retaining 32.0% of the signal. This has been further improved upon by altering the cuts and seeing how they affect confidence limits, reducing the background to 1.4% while retaining 22.3% signal. An estimate of the systematics has also been attempted by fitting various equations to the Monte Carlo data set and finding the difference between them and then applied the data in order to find the signal scale factor required for discovery.

Further analysis could be performed on each of the production methods shown in figure 1 using a similar method. This would increase the total number of signal events and therefore reduce the final signal scale factor. This would require a similar analysis to the one outlined in this paper but with different backgrounds and therefore a different treatment of the cuts applied.

References

[1]   URL: http://atlas.web.cern.ch/Atlas/GROUPS/MUON/mag%0Celd/.

[2]   URL: http://hedberg.web.cern.ch/hedberg/home/atlas/atlas.html.

[3]   G. Aad et al. "The ATLAS Inner Detector commissioning and calibration". In: *Eur. Phys. J.* C70 (2010), pp. 787–821. DOI: 10.1140/epjc/s10052-010-1366-7. arXiv: 1004.5293 [physics.ins-det].

[4]   Georges Aad et al. "Combined Measurement of the Higgs Boson Mass in pp Collisions at $\sqrt{s} = 7$ and 8 TeV with the ATLAS and CMS Experiments". In: *Phys. Rev. Lett.* 114 (2015), p. 191803. DOI: 10.1103/PhysRevLett.114.191803. arXiv: 1503.07589 [hep-ex].

[5]   Georges Aad et al. "Monitoring and data quality assessment of the ATLAS liquid argon calorimeter". In: *JINST* 9 (2014), P07024. DOI: 10.1088/1748-0221/9/07/P07024. arXiv: 1405.3768 [hep-ex].

[6]   Georges Aad et al. "Observation of a new particle in the search for the Standard Model Higgs boson with the ATLAS detector at the LHC". In: *Phys. Lett.* B716 (2012), pp. 1–29. DOI: 10.1016/j.physletb.2012.08.020. arXiv: 1207.7214 [hep-ex].

[7]   Georges Aad et al. "Search for the Standard Model Higgs boson decay to $\mu^+\mu^-$ with the ATLAS detector". In: *Phys. Lett.* B738 (2014), pp. 68–86. DOI: 10.1016/j.physletb.2014.09.008. arXiv: 1406.7663 [hep-ex].

[8]   S. Agostinelli et al. "GEANT4: A Simulation toolkit". In: *Nucl. Instrum. Meth.* A506 (2003), pp. 250–303. DOI: 10.1016/S0168-9002(03)01368-8.

[9]   A. et al. Airapetian. *ATLAS detector and physics performance: Technical Design Report, 1.* Technical Design Report ATLAS. Geneva: CERN, 1999. URL: https://cds.cern.ch/record/391176.

[10]   *ATLAS liquid-argon calorimeter: Technical Design Report.* Technical Design Report ATLAS. Geneva: CERN, 1996. URL: http://cds.cern.ch/record/331061.

[11]   "ATLAS muon spectrometer: Technical design report". In: (1997).

[12]   D. Binosi et al. "JaxoDraw: A Graphical user interface for drawing Feynman diagrams. Version 2.0 release notes". In: *Comput. Phys. Commun.* 180 (2009), pp. 1709–1715. DOI: 10.1016/j.cpc.2009.02.020. arXiv: 0811.4113 [hep-ph].

[13]   R. Brun and F. Rademakers. "ROOT: An object oriented data analysis framework". In: *Nucl. Instrum. Meth.* A389 (1997), pp. 81–86. DOI: 10.1016/S0168-9002(97)00048-X.

[14]   Serguei Chatrchyan et al. "Evidence for the 125 GeV Higgs boson decaying to a pair of τ leptons". In: *JHEP* 05 (2014), p. 104. DOI: 10.1007/JHEP05(2014)104. arXiv: 1401.5041 [hep-ex].

[15]   Nathaniel Craig, Jamison Galloway, and Scott Thomas. "Searching for Signs of the Second Higgs Doublet". In: (2013). arXiv: 1305.2424 [hep-ph].

[16]   A. Denner et al. "Standard Model Higgs-Boson Branching Ratios with Uncertainties". In: *Eur. Phys. J.* C71 (2011), p. 1753. DOI: 10.1140/epjc/s10052-011-1753-8. arXiv: 1107.5909 [hep-ph].

[17]   Avital Dery et al. "What if $BR(h --> \mu\mu)/BR(h --> \tau\tau)$ does not equal m_μ^2/m_τ^2?". In: *JHEP* 05 (2013), p. 039. DOI: 10.1007/JHEP05(2013)039. arXiv: 1302.3229 [hep-ph].

[18] Johannes Haller. "The First-level trigger of ATLAS". In: *PoS* HEP2005 (2006), p. 391. arXiv: `physics/0512195 [physics]`.

[19] Thomas Junk. "Confidence level computation for combining searches with small statistics". In: *Nucl. Instrum. Meth.* A434 (1999), pp. 435–443. DOI: `10.1016/S0168-9002(99)00498-2`. arXiv: `hep-ex/9902006 [hep-ex]`.

[20] Vardan Khachatryan et al. "Search for a standard model-like Higgs boson in the $\mu^+\mu^-$ and e^+e^- decay channels at the LHC". In: *Phys. Lett.* B744 (2015), pp. 184–207. DOI: `10.1016/j.physletb.2015.03.048`. arXiv: `1410.6679 [hep-ex]`.

[21] L Rossi and O Brüning. *High Luminosity Large Hadron Collider A description for the European Strategy Preparatory Group.* Tech. rep. CERN-ATS-2012-236. Geneva: CERN, Aug. 2012. URL: `https://cds.cern.ch/record/1471000`.

[22] Antonio Salvucci. "Measurement of muon momentum resolution of the ATLAS detector". In: *EPJ Web Conf.* 28 (2012), p. 12039. DOI: `10.1051/epjconf/20122812039`. arXiv: `1201.4704 [physics.ins-det]`.

[23] Pekka K. Sinervo. "Signal significance in particle physics". In: *Advanced statistical techniques in particle physics. Proceedings, Conference, Durham, UK, March 18-22, 2002.* 2002, pp. 64–76. arXiv: `hep-ex/0208005 [hep-ex]`. URL: `http://www.ippp.dur.ac.uk/Workshops/02/statistics/proceedings//sinervo.pdf`.

[24] Stefan Weinzierl. "Introduction to Monte Carlo methods". In: (2000). arXiv: `hep-ph/0006269 [hep-ph]`.

A Significance Graphs

This section contains all the significance against cut value plots used to calculate the optimum cut values.
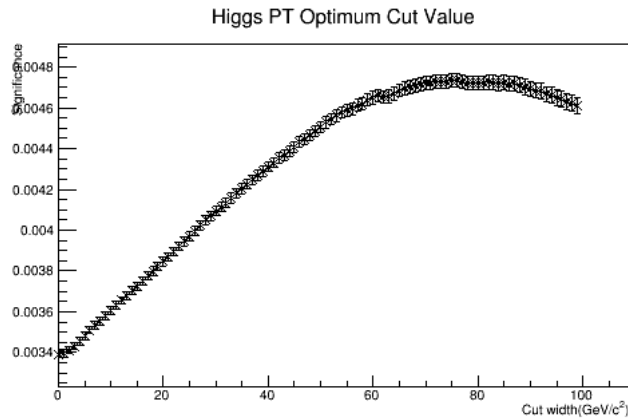

Figure 16: Optimum cut value using significance on Higgs transverse momentum
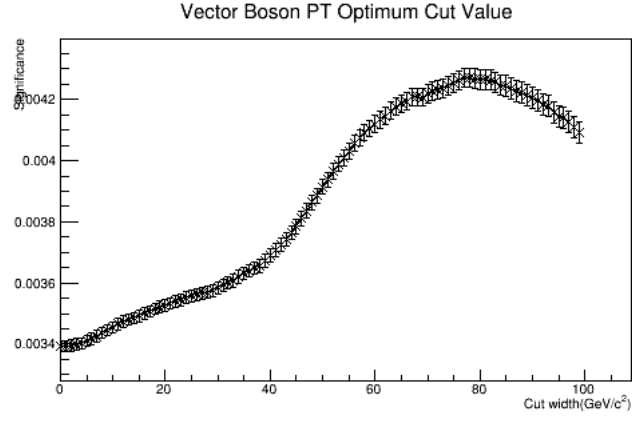
23

Figure 17: Optimum cut value using significance on the transverse momentum of the vector boson
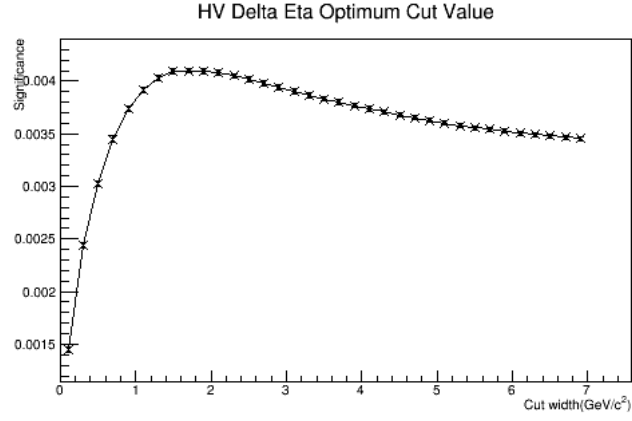

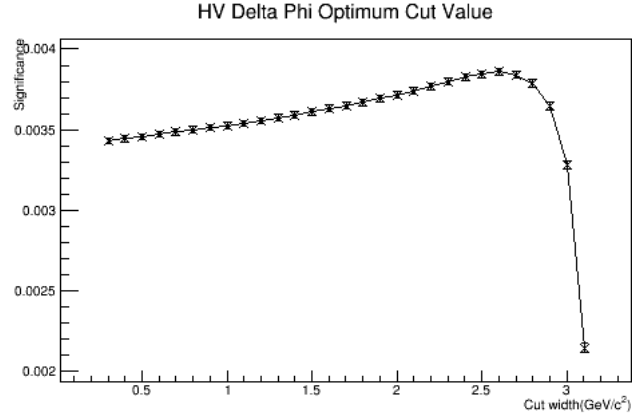Figure 18: Optimum cut value using significance on $\Delta\eta$ between Higgs and the vector boson

Figure 19: Optimum cut value using significance on $\Delta\phi$ between Higgs and the vector boson
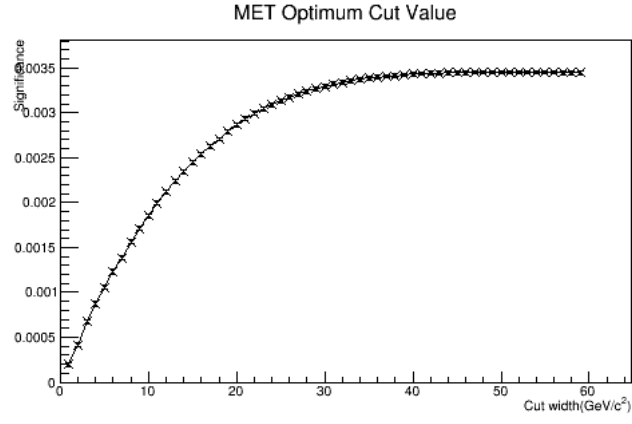
24

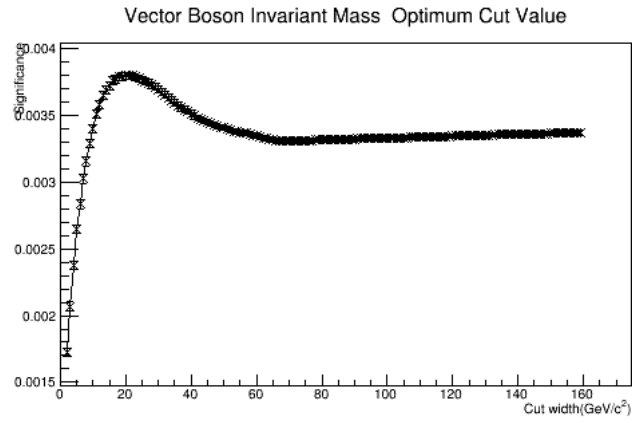Figure 20: Optimum cut value using significance on MET

Figure 21: Optimum cut value using significance on the invariant mass of the jets (vector boson)